macQsimal	Title **Micro-optical OPM physics package and encapsulation report**	Deliverable Number **D4.4**
Project Number **820393**		Version **1.0**

H2020-FETFLAG-2018-2021

macQsimal

Miniature Atomic vapor-Cell Quantum devices for SensIng and Metrology AppLications

Deliverable D4.4

Micro-optical OPM physics package and encapsulation report

WP4 – Miniature optically-pumped magnetometers

Authors: Vito Giovanni Lucivero (ICFO), Jakob Reichel (CNRS)

Lead participant: CNRS

Delivery date: 07.03.2021

Deliverable type: Report

Dissemination level: Public

This work has received funding from the European Union's Horizon 2020 research and innovation programme under grant agreement No. 820393.

Revision History

Author Name, Partner short name	Description	Date
Vito Giovanni Lucivero (ICFO)	Start of document	04.11.2020
Vito Giovanni Lucivero (ICFO)	Update of the document	16.09.2021
Vito Giovanni Lucivero (ICFO)	Update of the document	11.10.2021
Vito Giovanni Lucivero (ICFO)	Update of the document	13.10.2021
Jakob Reichel (CNRS)	Update of the document	21.10.2021
Vito Giovanni Lucivero (ICFO)	Implemented comments	27.10.2021
Philipp Treutlein (UNIBAS)	Review	03.11.2021
Jakob Reichel (CNRS)	Final draft version	09.11.2021
Johannes Ripperger (accelCH)	Final formal checks and layout	10.11.2021
Jakob Reichel (CNRS)	Final version (v1.0)	07.03.2022

Abbreviations

accelCH	accelopment Schweiz AG *(macQsimal Beneficiary No. 3)*
ASN	Atomic shot noise
BAE	Back-action evading
CNRS	Centre National de la Recherche Scientifique CNRS *(participating in macQsimal with the Laboratoire Kastler Brossel, LKB, macQsimal Beneficiary No. 6)*
CSEM	CSEM Centre Suisse d'Electronique et de Microtechnique SA – Recherche et Development *(Beneficiary No. 1 and Coordinator of the macQsimal project)*
DAQ	Data acquisition card
EOM	Electro-optical modulator
FID	Free-induction decay
ICFO	Fundacio Institut de Ciencies Fotoniques *(The Institute of Photonic Sciences, macQsimal Beneficiary No. 4)*
MEG	Magnetoencephalography
MCG	Magnetocardiography
MEMS	Micro electro-mechanical systems
NV	Nitrogen-vacancy
OPM	Optically-pumped magnetometer
PID	Proportional integral derivative
PDH	Pound-Drever-Hall
QND	Quantum non-demolition
SERF	Spin exchange relaxation-free
SOA	State-of-the-art
TIA	Transimpedance amplifier

Contents

1 OVERVIEW 5

1.1 State-of-the-art and goals 5

1.2 Multi-pass and cavity-enhanced OPM 6

2 CAVITY MICROCELL WORKING PRINCIPLE AND MEASUREMENT SCHEMES 7

2.1 Measurement scheme in transmission (Faraday rotation) 8

2.1.1 Simulated signals with Faraday rotation 10

2.2 Measurement in reflection (Pound-Drever-Hall) 10

2.2.1 Simulated signals in reflection 12

3 PARAMETER OPTIMIZATION IN MICRO-OPTICAL OPMS 13

3.1 Transit time and optimal buffer gas pressure 13

3.2 Fundamental sensitivity 15

3.3 Pressure-induced glass bending 16

4 DESIGN AND FABRICATION OF PLANAR CAVITY MICROCELLS 18

4.1 Designs of planar cavity microcell 18

4.2 Fabrication steps 19

4.3 Coating of the microcells 20

5 BIBLIOGRAPHY 21

1 Overview

1.1 State-of-the-art and goals

The realization of a sub-mm active volume OPM has both applied and fundamental interest. Reducing the volume of high-sensitivity atomic sensors is a technological challenge for numerous applications in space science and navigation as well as in biomedical diagnostics. A comprehensive review on chip-scale atomic sensors has been recently reported [1], describing how most solutions still make use of mm-size active volumes, combined in more compact devices through anodic bonding with silicon wafers or integrated on the top of photonic waveguides to interact with their evanescent field. Further size reduction and flexibility can significantly improve the spatial resolution of high-sensitivity OPMs in applications like MEG and MCG as well as in the study of materials/solid-state magnetic fields. In Figure 1 we report a review of magnetic sensors with state-of-the-art sensitivity and their characteristic length. The objective of the described WP4 (*Miniature optically-pumped magnetometers*) is twofold. The first one is to reduce the size of OPMs down to sub-mm interaction length to perform magnetic microscopy with sub-mm spatial resolution, as depicted in Figure 2. The cavity microcells introduced here will compete with NV-centers based sensors, which usually achieve much better spatial resolution, below 1 µm, but show sensitivity in the pico-Tesla level only. The second objective is to quantum-enhance the micro-OPM sensitivity below what is classically achievable. In fact, atomic sensors with sub-mm active volumes will show higher ASN which is expected to be the dominant noise contribution over technical noise sources. To keep the sensitivity high, multi-pass [2] or cavity geometries [3] will be necessary to enhance the optical depth of atomic vapours enclosed in microcells. The combination of sub-mm active volume with cavity-enhanced optical depth will make this device a unique platform to study spin squeezing and QND measurements for quantum-enhanced miniaturized OPMs. In this deliverable we describe the design optimization and the strategy towards the development of cavity microcells. This work has recently resulted in the filing of an EP patent P0118EP00.

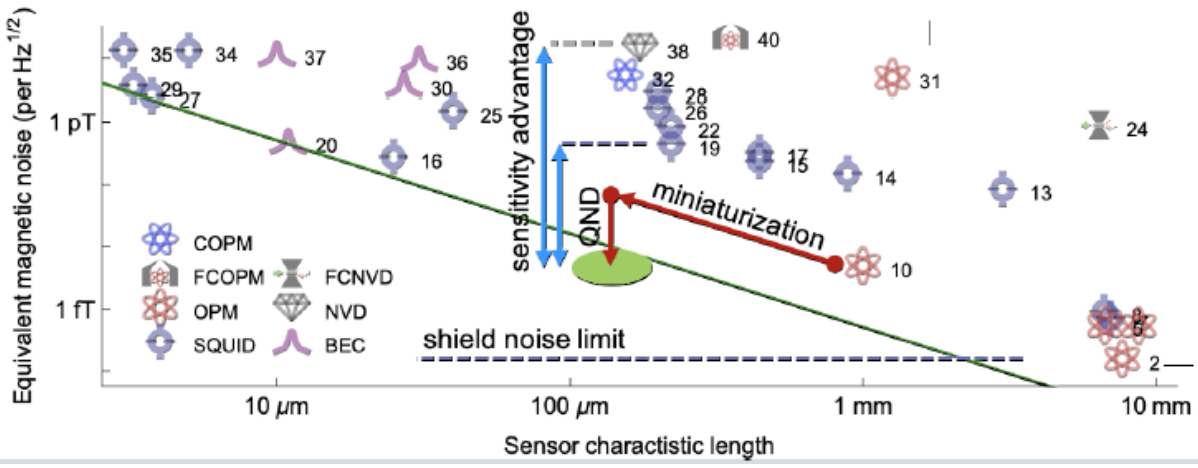

Figure 1: State-of-the-art sensors.

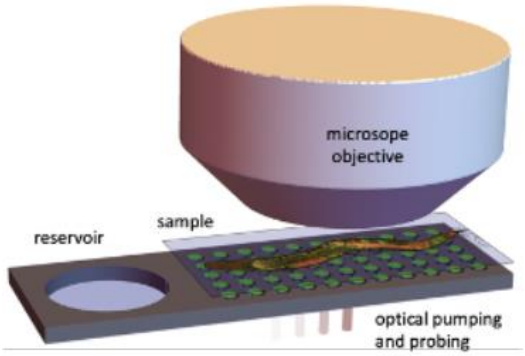

Figure 2: Pictorial application of cavity-enhanced micro-optical OPMs to magnetic microscopy. The magnetic characterization of a sample, placed on the top of the cavity microcell, can be obtained by probing a single cavity with measurement in reflection, while performing conventional microscopy at the same site. A scan of the system consisting of microcell and sample would allow one to probe multiple cavities for a full 2D magnetic microscopy characterization of samples at sub-mm scale.

1.2 Multi-pass and cavity-enhanced OPM

Recent SOA sensitive scalar OPMs use multi-pass geometries to increase the interaction length by 2 orders of magnitude, reaching sub-fT sensitivity [2], quantum-noise-limited operation in Earth's field [4] and applications in MEG and MCG in unshielded environment [5]. These SOA sensors are based on enhancement of dispersive Faraday rotation thanks to the increased optical depth for an off-resonant probe. The fabrication process consists of active alignment and anodic bonding between mirrors and Pyrex glass with mm to cm active volume. These hybrid cells are fitted with a filling tube, through which they are evacuated and filled with Rb and N_2 with conventional glassblowing techniques. The filling tube, i.e., the cell stem, is finally sealed by heating. In configurations with cylindrical or spherical mirrors [2] [6], the probe beam is focused into a 100 μm hole through one mirror, then it expands within the interaction area and exit after multiple reflections, through the same hole. In geometries with planar mirrors [5], these are cut and relatively shifted to allow a beam with near-zero input angle to undergo multiple reflections and leave the cell. Multi-pass geometries have several advantages like deterministic number of passes and optical length, high input/output power ratio and the possibility of combining an interaction region where the beams expand and overlap with a different one where they are well-separated, in contrast to typical standing wave cavities. The latter feature has been recently used in a direct gradiometer with a single multi-pass cell [7] and allows the atoms to interact with a wide beam region excluding strongly focused areas, that would induce decoherence due to atomic diffusion [8], limiting the possibility of quantum enhancement by spin squeezing.

However, the fabrication techniques of multi-pass cells become increasingly difficult when the active volume is reduced to sub-mm dimensions. The implementation of technologically available micro-optics and micro-cavities is an attractive and promising solution. To date, cavity-enhanced atomic sensing techniques have been applied to non-magnetic transitions in atomic systems [9], of interest for atomic clocks, and in an amplitude-modulated nonlinear optical rotation (AMOR) magnetometer [3]. The latter is an absorptive measurement where, due to optically-induced atomic alignment, in the presence of a magnetic field the atomic medium works like a rotating polarizer causing a rotation in a linearly polarized probe. Our new approach in D4.4 is to cavity-enhance a dispersive Faraday rotation in the presence of high degree of atomic orientation, similarly to SOA multi-pass sensors, but considering a sub-mm active volume OPM. Cavity-enhancement of dispersive linear Faraday effect [10], for a unpolarized ensemble, has been recently reported within the macQsimal consortium.

2 Cavity microcell working principle and measurement schemes

In Figure 3 we show the general scheme of a cavity microcell. The full cavity microcell length is $\mathbf{L=L_1+L_2+L_3}$. The first glass substrate can have thickness $\mathbf{L_1}$ ranging between 100 µm and few mm, depending on the desired cavity free spectral range $\boldsymbol{\Delta\nu_{FSR} = c/2L}$. The middle silicon wafer has sub-mm thickness $\mathbf{L_2}$, e.g., 100 or 200 µm, to enable sub-mm interaction length and spatial resolution. The second glass substrate also has sub-mm thickness $\mathbf{L_2}$, e.g., 200 µm, allowing for sub-mm stand-off distance from a sample. Here we briefly explain the physics of the cavity-enhanced magnetometry for a single probe beam interacting with the cavity microcell after optical pumping.

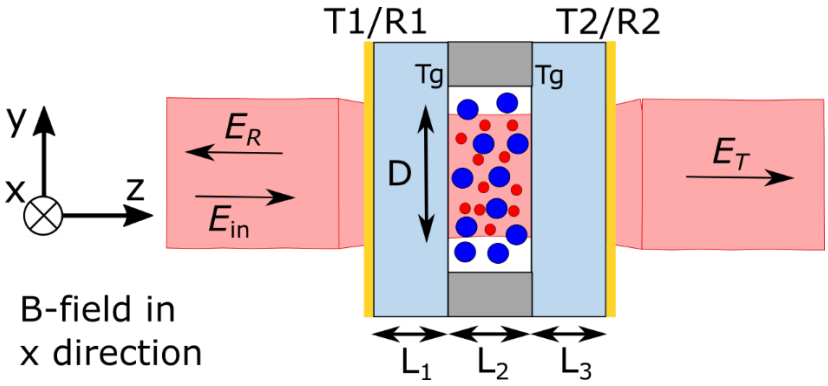

Figure 3: Cavity microcell sketch and dimensions.

The input probe field E_{in} can be linearly polarized for detection in transmission (Section 2.1) or circularly polarized with σ^+ or σ^- polarization (Section 2.2) for detection in reflection, while E_T (E_R) is the transmitted (reflected) electric field. The probe beam diameter D is twice the waist radius at the center of the atomic interaction length $\mathbf{L_2}$ (the thin silicon wafer thickness). The optical cavity for the probe is generated by optical coating the outer surfaces of the glass substrates with reflectance R1 (T1=1-R1) and R2 (T2=1-R2), respectively (we consider a reflectance R_G (Tg=1-Rg) for the inner surfaces).

In Section 4 we describe in detailed designs and fabrication steps of cavity microcells. Here we anticipate that the microcells can have multiple sensing chambers, as shown in Figure 4, to perform differential measurements between different confining chambers, i.e., in a magnetic gradiometer operation mode.

Figure 4: Cavity microcell with reservoir and multiple sensing round chambers.

As described in Sections 2.1 and 2.2, in our methods pump and probe are collinear and pulsed optical pumping (Bell-Bloom like) generates high atomic polarization $P_z = 2\langle S_z\rangle$, where $\langle S_z\rangle$ is the averaged electron spin component along the pump/probe direction z, transverse with respect to the magnetic field $\vec{B}$ to be measured, which points in the x direction. Pump and probe are meant to work at different frequencies, e.g., the pump on resonance with the D1 line (795 nm) and the probe far-detuned, $\Delta > 10$ GHz, from the D2 line (780 nm). After the pump laser is switched off, atomic spins freely precess in the transverse x-y plane at the Larmor frequency $\omega_L = \gamma B_x$ before relaxation, so that $P_z(t) = P_z(0)\ \cos(\omega_L t)\, e^{-\frac{t}{T_2}}$, where γ is the alkali gyromagnetic ratio and T_2 is the transverse relaxation time. The magnetic field magnitude is obtained from a highly sensitive measurement of the Larmor frequency, since the gyromagnetic ratio is known. The presence of the atomic ensemble as well as the atomic polarization evolution modify the interaction length, hence the total cavity microcell optical path length, by $\mathbf{L2 \rightarrow n^{\pm} L2}$ where n^+ and n^- are the indexes of refraction for σ^+ and σ^- circular polarization respectively. These are given, as a function of probe linear frequency ν and time, by:

$$n^+(\nu, t) = 1 + \left(\frac{P_z(t)}{2} + 1\right) \times \frac{n r_e c^2 f_{osc}}{4\nu} D(\nu) \qquad \text{Eq. 1a}$$

$$n^-(\nu, t) = 1 + \left(1 - \frac{P_z(t)}{2}\right) \times \frac{n r_e c^2 f_{osc}}{4\nu} D(\nu) \qquad \text{Eq. 1b}$$

where n is the atomic number density, r_e is the electron radius, c is the speed of light, f_{osc} is the oscillation strength of the rubidium D_2 line and $D(\nu) = (\nu - \nu_0)/\left[(\nu - \nu_0)^2 + (\frac{\Gamma}{2})^2\right]$ is a dispersion profile centered at the ν_0 atomic resonance, e.g. the central D2 line, with buffer gas pressure broadened linewidth Γ.

2.1 Measurement scheme in transmission (Faraday rotation)

In the **detection in transmission method** the probe is linearly polarized and locked on resonance with the cavity microcell at frequency ν_{cav}, but far detuned from atomic resonance, $\Delta = \nu_{cav} - \nu_0 \gg 10$ GHz. After propagation through the atomic interaction length L_2, the input electric field E_{in} becomes $E_{out} = E_{in}$ $(\cos(\phi)\,\hat{x} - \sin(\phi)\,\hat{y})$ undergoing paramagnetic Faraday rotation $\phi(t) = \phi_0 \sin(\omega_L t)\, e^{-\frac{t}{T_2}}$, where the maximum rotation amplitude is:

$$\phi_0 = \frac{n r_e f_{osc}}{2\Delta} G(\mathcal{F}) L_2 P_x \qquad \text{Eq. 2}$$

Here we introduce $G(\mathcal{F}) > 1$ as the cavity-enhanced gain due to the optical cavity with finesse $\mathcal{F}$, in contrast with the single-pass scenario where $G(\mathcal{F}) = 1$.

In Figure 5 we show the measurement scheme for an optically-pumped magnetic gradiometer in transmission. Pump and Probe lasers are fiber coupled and collimated in a collinear operation mode. Alternatively to fiber coupling, the two lasers can propagate in free space and be aligned in the same mode through a dichroic mirror. Collinear pump and probe beams propagate along the z axis, transverse with respect to the magnetic field to be measured in the x direction and to the long side of the cavity microcell. The cavity microcell is heated to increase the atomic density in the device to the desired value and the temperature is stabilized using a sensor-feedback system, e.g., a thermocouple and a PID circuit.

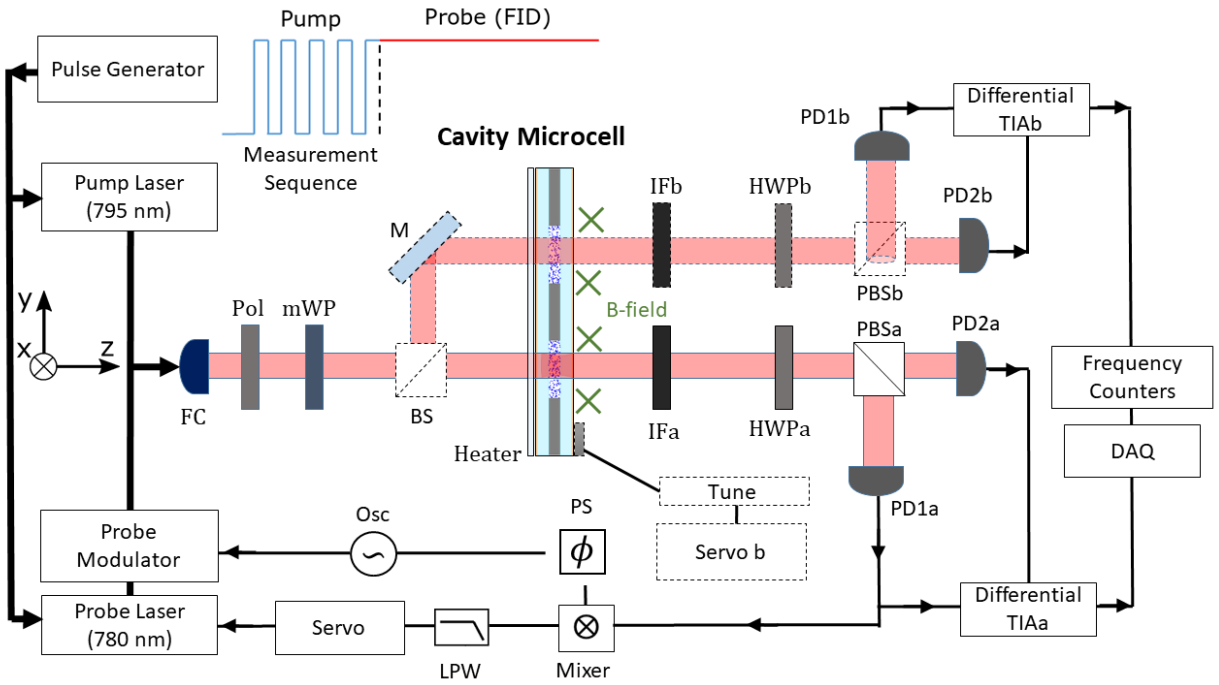

Figure 5: Optically-pumped magnetic gradiometer with a cavity microcell in transmission.

In the transmission measurement scheme a linear polarizer purifies the input polarization before a multi-order waveplate linearly polarize the probe (e.g., 780 nm) and circularly polarize the pump beam (e.g., 795 nm). In a gradiometer mode a beam splitter and a reflective mirror separate the single mode in two parallel beams, giving effectively two copies of the same optical system. This can be repeated providing multiple parallel beams for higher order gradiometer mode. Alternatively, one can use a single beam and multi-element photodiode, e.g., a quadrant photodiode with four active areas, or an array of photodiodes. From now on we describe the simple option with two parallel beams, top and bottom with respect to the y-direction, each comprising collinear pump and probe. The pulsed pump beam can last from few microseconds to milliseconds, depending on available power, impinges on the atomic ensemble in the microcell and its residual is absorbed by interference filters that, on the other hand, transmit probe light. Top/Bottom probe beams propagate through the cavity microcell undergoing cavity-enhanced Faraday rotation, which is detected by conventional balanced polarimeters. Each one consists of a half-wave plate polarizing beam splitter and two photodiodes. The signals are subtracted and amplified in each polarimeter by a differential transimpedance amplifier TIA. The outputs, the two gradiometer channels, are fed into a data acquisition card (DAQ) or to frequency counters where a final differential measurement is performed. The signal is processed with suitable software and electronics to obtain Larmor frequency, magnetic field value and noise floor for each channel as well as magnetic field gradient with sub-mm spatial resolution and a baseline given by the distance between the two beams. The magnetic noise floor is obtained in the frequency domain by repeating the same pump-probe measurement sequence, driven at a frequency set by the pulse generator. One photodiode, e. g. is used for continuously lock the probe laser frequency to the cavity length, via a PDH feedback circuit. The probe is modulated, e.g., by an electro optical modulator (EOM), with a driving oscillator so that the photodiode output is mixed with the main oscillator using a low-pass filter, a mixer and a phase shifter to give an error signal centred around the cavity microcell resonance. A servo, e.g., PID controller, provides feedback to the probe laser current in order to keep the laser frequency locked to the cavity resonance frequency, which is far-detuned from the atomic resonance, $\Delta > 10$ GHz, to avoid probe absorption. An additional servo system can work as secondary feedback to a system, e.g., piezo-electric transducer or additional thin film heater, for fine cavity tuning.

2.1.1 Simulated signals with Faraday rotation

In Figure 6 we show exemplary transmitted intensity (left) and cavity-enhanced Faraday rotation (right) for one optically-pumped magnetic gradiometer channel. In the first graph, the probe frequency is scanned around cavity resonance (dashed red), far-detuned from atomic resonance ($\Delta = 95$ GHz). This signal is used to generate the PDH to lock the laser frequency on resonance. The microcavity-enhanced Faraday rotation signal in transmission is shown in the second graph. In particular, we simulate two cavity conditions with second glass substrate reflectance R2=99% and first glass reflectance R1=90% (gold) and R1=97% (blue), giving a cavity finesse of about 50 and 150, respectively. In the second case the gain in Faraday rotation is also higher, giving two orders of magnitude signal improvement (blue), with respect to a single pass (green) through L_2 = 200 μm. The reflectance of the substrates can vary in different embodiments, to optimize the trade-off between high-finesse and residual probe beam absorption. In the inset of Figure 6 (right) we plot the same Faraday rotation signals over 0.5 m to show clear polarization oscillations at the Larmor frequency $\omega_L = \gamma B_x$. The differential measurement between the two channels in a frequency counter provides the magnetic gradiometer signal.

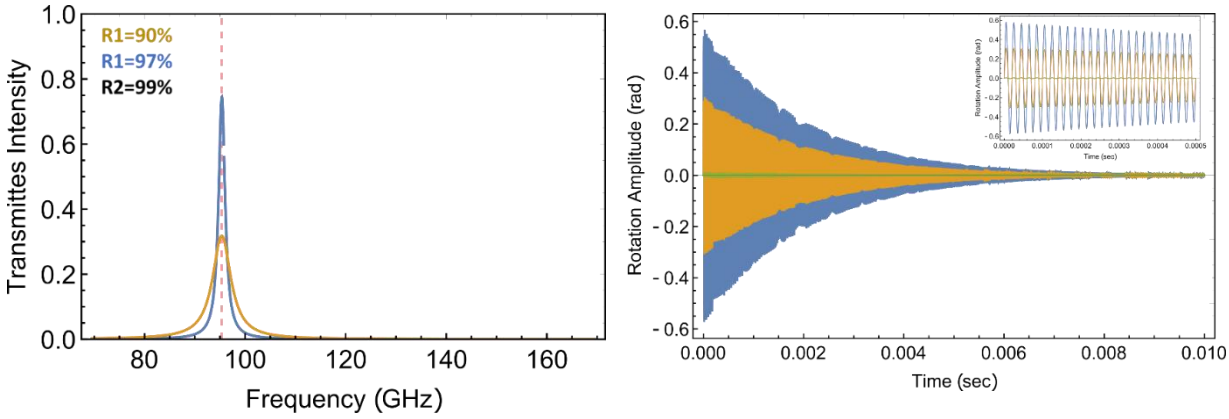

Figure 6: (Left) Transmitted intensity versus laser frequency. (Right) Faraday rotation FID signal for different cavity finesse.

2.2 Measurement in reflection (Pound-Drever-Hall)

While cavity-enhancement of Faraday rotation in transmission is promising for experimental realization [10], there are some non-trivial aspects like degeneracy of cavity resonance for different linear polarizations and interference with the reflected beam that justify the study of different approaches. Here we propose a solution based on Pound-Drever-Hall (PDH) laser locking to a cavity in reflection [11] with the same cavity surfaces and transmittances shown in Figure 3. In Figure 7 we show the proposed setup. A 795 nm pulsed laser induces atomic polarization, not much affected by the cavity due to the strong on-resonance absorption, and weak reflectivity of the cavity mirrors at this wavelength. A circularly polarized 780 nm probe is used for Pound-Drever-Hall (PDH) measurement and stabilization of the laser frequency relative to the cavity resonance.

In Figure 8 we report an exemplary reflected intensity and microcavity-enhanced PDH error signal for one gradiometer channel. The top/left figure shows the reflected intensity around a cavity resonance frequency corresponding to far-detuning (Δ=95 GHz) from atomic resonance. This is used to generate the PDH error signal shown in the bottom/left figure, with frequency sidebands due to the probe phase modulation by an electro-optical modulator (EOM). The PDH locking technique is a well-established metrology strategy to lock the laser frequency to a cavity resonance, by generating an asymmetric error signal, with respect to the cavity condition [11].

In the **detection in reflection method** the probe is circularly polarized and locked on resonance with the cavity microcell at frequency ν_{cav}, again far detuned from atomic resonance, $\Delta = \nu_{cav} - \nu_0 \gg 10\ \mathrm{GHz}$. In this configuration, the atomic polarization induced displacement $L2' \rightarrow n^{\pm}(t)L2$ is measured by detecting the reflected intensity $|E_R|^2$ in a photodiode, whose signal is fed into a PDH frequency locking system to generate an error signal. When the laser frequency is close to cavity resonance, the error signal is proportional to the total cavity displacement $\Delta L = L2(n^{\pm} - 1)$ as well as to the cavity gain:

$$\varepsilon = DG(\mathcal{F})\delta\nu_{cav} \quad \text{with} \quad D = \frac{8\sqrt{P_c P_s}}{\delta\nu} \qquad \text{Eq. 3}$$

where $\delta\nu_{cav} = \nu'_{cav} - \nu_{cav} = -\frac{\nu'_{cav}}{L}\Delta L$ is the linear change in laser frequency following the cavity displacement ΔL, D is the usual PDH slope, P_c and P_s are the powers of carrier and first order sideband of the error signal, while $\delta\nu$ is the cavity microcell linewidth. We note that the cavity has the effect to enhance the error signal slope, as well as increasing carrier and sideband powers.

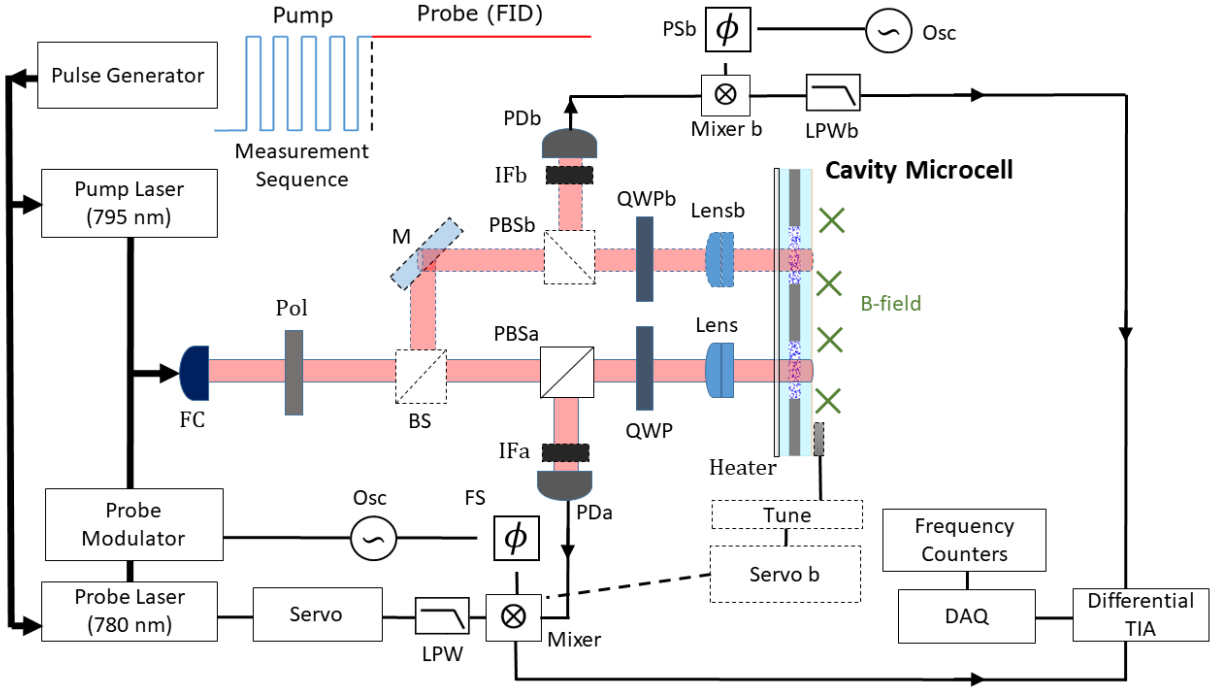

Figure 7: Optically-pumped magnetic gradiometer with a cavity microcell in reflection.

In Figure 7 we show the measurement scheme for an optically-pumped magnetic gradiometer in reflection. Here a polarizer purifies the input linear polarization of both pump and probe beams. As in the transmission method, in one possible gradiometer scheme a beam splitter and a reflective mirror split the single mode in two beams. In both top and bottom beams a polarizing beam splitter and a quarter waveplate circularly polarize both collinear pump and probe lasers. They can be collimated or focused by a lens, depending on the desired beam radius at atomic interaction. A lens can also be replaced by a system of lenses, i.e., a telescope, for fine beam shaping. In this method, the second glass substrate has a reflectance close to 1, e.g., 99,99%. The reflected probe outputs are collected by photodiodes PDa/PDb and fed into a PDH laser frequency locking system to generate an error signal for each gradiometer channel. Such system is essentially the same described in the transmission method, comprising: a probe modulator, e.g., an electro optical modulator (EOM), a driving oscillator, a mixer that combines the photodiode output with the main oscillator, a low-pass filter, and a phase shifter. The error signals are fed to a servo, e.g., PID controller, which provides a feedback, e.g., a dc voltage output, to the

probe laser current to keep the laser frequency on resonance, following the cavity microcell displacement ΔL. As previously described, an additional servo system can give a secondary feedback to a fine-tuning system applied to the cavity microcell.

The signal processing can occur at different stages, by directly processing the reflected intensity or from the PDH error signals, where both show precession at the Larmor frequency and relaxation. The gradiometer measurement and the common mode noise rejection occur via a transimpedance differential amplifier that subtract the error signals from the two channels. Its output is then fed to DAQ or frequency counter to process the magnetic gradiometer signal.

2.2.1 Simulated signals in reflection

In Figure 8 we report an exemplary reflected intensity and microcavity-enhanced PDH error signal for one gradiometer channel. The top/left figure shows the reflected intensity around a cavity resonance frequency corresponding to far-detuning ($\Delta = 95$ GHz) from atomic resonance. This is used to generate the PDH error signal shown in the bottom/left figure, with frequency sidebands due to the probe phase modulation by an electro-optical modulator (EOM).

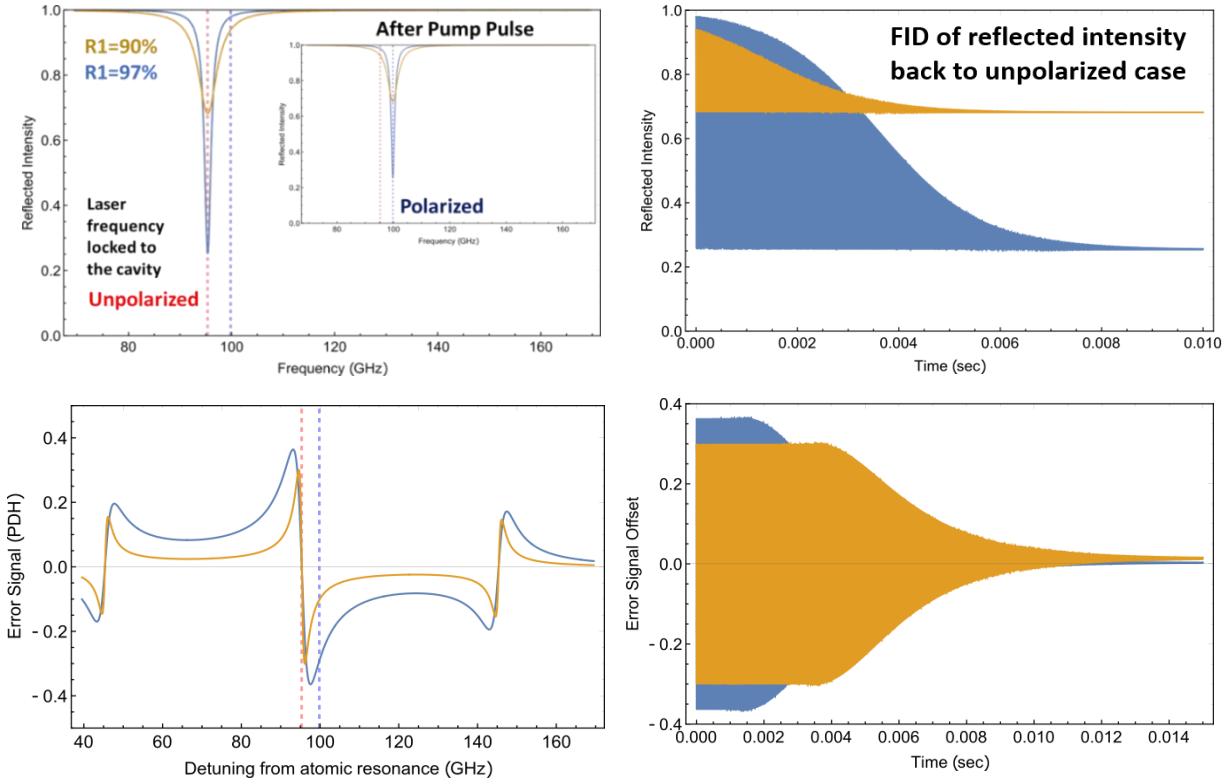

Figure 8: (Top/Left) Cavity-enhancement of atomic interaction by PDH detection in reflection. (Top/Right) Reflected intensity as the atoms depolarize. (Bottom/Left) PDH error signal as the laser is phase modulated. (Bottom/Right) Precession of the error signal offset during free induction decay.

The probe laser frequency is initially locked to the cavity with unpolarized atoms (dashed red). The optical pumping induces a shift of the cavity resonance condition (dashed blue) with following free-induction-decay back to the unpolarized resonance condition. As for transmission, we simulate two microcavity-enhanced conditions with second glass substrate reflectance R2=99% and first glass reflectance R1=90% (gold) and R1=97% (blue). In the top/right figure we show free-induction-decay of the reflected intensity for the two conditions with an amplitude improvement for higher finesse. Alternatively, we can use the precession of the error signal (bottom/right figure), which is proportional to the offset from cavity

resonance, to perform the magnetic field measurement. Note that the cavity enhancement increases the error signal slope and the decay time in the free-induction-decay of the error signal offset.

3 Parameter optimization in micro-optical OPMs

3.1 Transit time and optimal buffer gas pressure

Sub-mm atomic cells have been also proposed for realization of SI units, like time, on a chip. As shown in Figure 9 (taken from [12]), in small dimensions cells and photonic structures the transit time broadening of atoms across the laser beam increases drastically in absence of buffer gas. For applications where alkali Doppler-free features need to be resolved, like atomic spectroscopy and atomic clocks, a beam size between 10 μm and 1 mm is then favourable. However, evanescent field interrogation can be appropriate for combining photonic structures with sensing of Doppler-broadened transitions. A hybrid approach that expands the photonic waveguide mode to 50 μm for atomic interaction in a mm active volume cell has been recently used for 780 nm laser frequency stabilization with a stability of 10^{-11} [13].

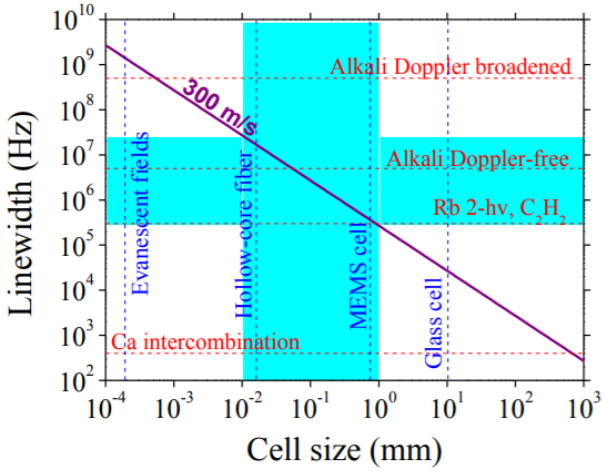

Figure 9: Transit time broadening at room temperature for vapour moving at 300 m/s. Figure from [12].

In OPMs, as well as in other atomic sensors, the transit time broadening is significantly reduced with the addition of inert buffer gas. This is also beneficial, by collisional mixing of excited states, for generation of high atomic polarization, optically-induced by depopulation pumping [14]. For sub-mm active volume, the buffer gas pressure needs to be optimized, similarly to MEMS cells, to balance the relaxation from the inner walls, inversely proportional to the N_2 pressure, and relaxation due to collisions between rubidium and buffer gas, proportional to its pressure.

The magnetic sensitivity of the cavity microcell, when used as an OPM, is proportional to the total relaxation Γ_{rel}:

$$\Gamma_{rel} = R_{WD} + R_{BG} + R_{SE} + R_{SD} \qquad \text{Eq. 4}$$

including spin-exchange R_{SE} and spin-destruction R_{SD} rates between Rb atoms and collisions with buffer gas R_{BG}. The first term due to relaxation rate with internal walls is particularly relevant in the cavity microcell, for sub-mm active volume, and is given by:

$$R_{WD} = \left[\left(\frac{\pi}{L}\right)^2 + \left(\frac{2.405}{r}\right)^2\right] \frac{D_0}{\eta} \sqrt{\frac{T}{273.15}} \qquad \text{Eq. 5}$$

where η is the nitrogen number density in multiples of one amagat n_0, D_0 is the diffusion constant at 273 K and 760 Torr (and thus 1 amg), while L and r are the cell length and beam waist (radius), respectively. The other terms are given explicitly by:

$$R_{BG} = n\sigma_{Rb-N_2}\bar{v}_{Rb-N_2} \quad \text{Eq. 6}$$

$$R_{SE} = q_{SE}n\sigma_{SE}\bar{v}_{Rb-Rb} \quad \text{Eq. 7}$$

$$R_{SD} = n\sigma_{SD}\bar{v}_{Rb-Rb} \quad \text{Eq. 8}$$

where n is the Rb number density, $\bar{v}_{Rb-N_2}(\bar{v}_{Rb-Rb})$ is the Rb-N2 (Rb-Rb) relative thermal velocity, $q_{SE} = 7/32$ is a reduction factor of spin-exchange due to nuclear spin [14], $\sigma_{Rb-N_2} = 1 \times 10^{-22}\ \mathrm{cm}^2$, $\sigma_{SE} = 1.9 \times 10^{-14}\ \mathrm{cm}^2$, $\sigma_{SD} = 1 \times 10^{-17}\ \mathrm{cm}^2$ are the Rb-N2, Rb-Rb spin-exchange and Rb-Rb spin-destruction collisional cross-sections [14], respectively.

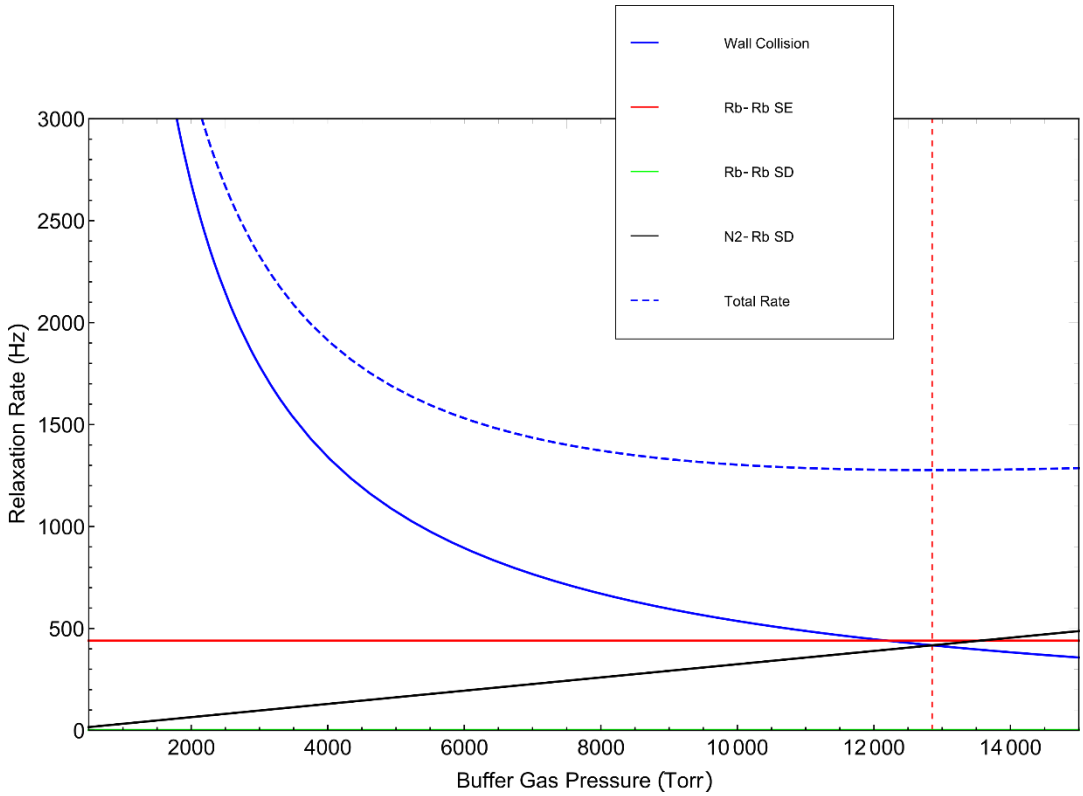

Figure 10: Relaxation rates vs buffer gas pressure.

As optimization example for the cavity microcell, in Figure 10 we show different contributions by wall collisions (blue), N2-Rb spin-destruction (black), Rb-Rb spin-exchange (red) and total relaxation rate (dashed-blue) for an interaction length **L_2=200 µm** and a beam diameter D=2r= 400 µm. In the presence of spin-exchange collisions, at a temperature of T=120°C, a plateau starts at about 10 bar with a minimum relaxation rate of about 1.2 kHz, at about 17 bar. For operation near-zero magnetic field, in the spin-exchange-relaxation-free (SERF) regime, the contribution from spin-exchange collisions is negligible and the cavity microcell can be used at higher temperatures, e.g., giving lower intrinsic relaxation rate. The cavity microcell can be used both in SERF and total field magnetometer mode and the optimal buffer gas pressure ranges from few bar (**L_2** = 1 mm) up to 20 bar (**L_2** =100 µm). All intermediate cases are covered by this design and fabrication technique.

Here we are not limiting the strategy to the SERF operation mode, since total field gradiometers based on the subtraction of FID signals from two atomic interaction regions can give comparable sensitivity in detecting biological signals with the great advantage of working in unshielded environment [5]. Furthermore, FID signals are suitable for continuous QND and BAE measurements when atomic spins freely precess in the transverse plane, along the probe propagation direction [15, 16].

3.2 Fundamental sensitivity

For N spin-1/2 atoms with coherence time $T_2 = 1/\Gamma_{rel}$, the fundamental sensitivity is limited by the ASN and, after a time of measurement much longer than coherence time $t \gg T_2$ is given by [2]:

$$\delta B = \frac{1}{\gamma}\sqrt{\frac{2e}{NT_2 t}} \qquad \text{Eq. 9}$$

where $2\pi/\gamma$ is the gyromagnetic ratio in units of T/Hz.

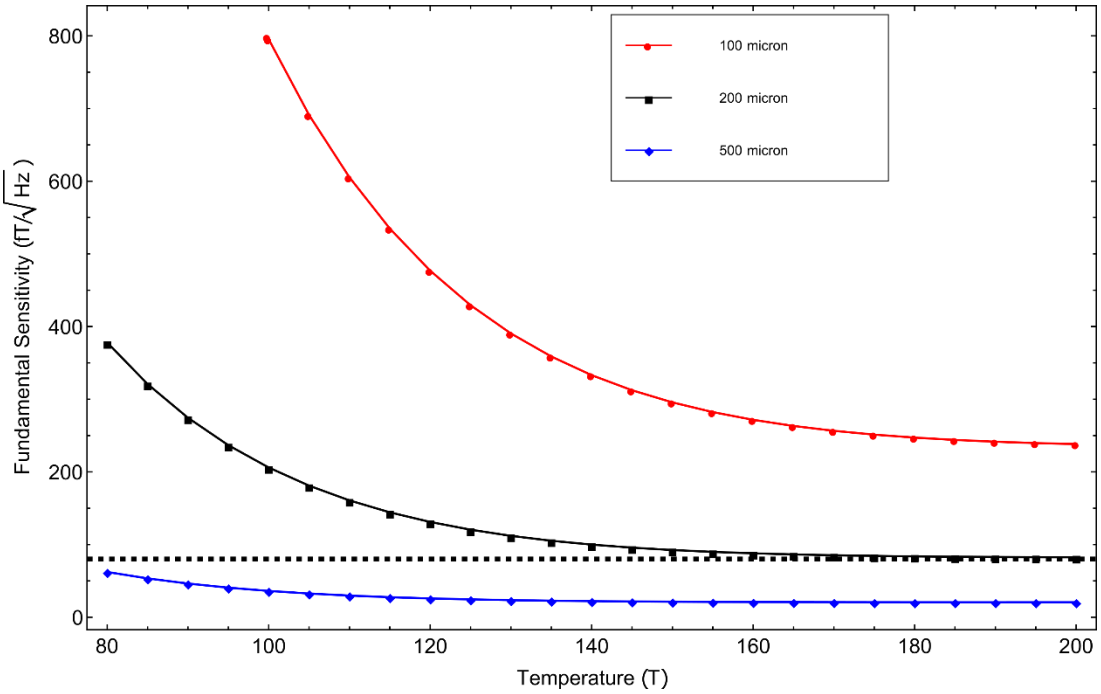

Figure 11: Projection-noise-limited sensitivity for a sub-mm interaction length of 100, 200 and 500 µm.

Since the total number of atoms N = nV is linear in each number density n and volume V, we can define the fundamental magnetic sensitivity per unit of volume in units of $\mathrm{Tcm}^{3/2}/\sqrt{\mathrm{Hz}}$:

$$\delta B_n = \frac{10^3}{\gamma}\sqrt{\frac{2e\,\Gamma_{rel}}{nt}}. \qquad \text{Eq. 10}$$

With the optimal relaxation rate of $\Gamma_{rel} = (2\pi)$ x 1.2 kHz, obtained in the previous section at T=120°C, in the presence of high buffer gas pressure and spin-exchange collisions, by using Eq. 10, we calculate that a sensor with sub-mm active volume of V= $\pi r^2 L = \pi\,(200\ \mu m)^3$ would have a fundamental sensitivity of 130 $\mathrm{fT}/\sqrt{\mathrm{Hz}}$ and a volume-adjusted sensitivity of sub- $\mathrm{fTcm}^{3/2}/\sqrt{\mathrm{Hz}}$, as shown in Figure 12, where we report Eq. 22 as function of temperature in °C . This optimal volume-adjusted sensitivity is comparable with state-of-the-art (SOA) sensitivity per unit of volume, obtained in a sub-femtotesla scalar magnetometer with two multi-pass cells with volume of 0.3 cm^3 each [2]. Then, while the absolute

sensitivity may limit the magnitude of magnetic field that could be detected, a sub-mm active volume OPM could have a fundamental ASN in the pico-tesla regime, which is attractive for quantum enhancement by QND and BAE measurements.

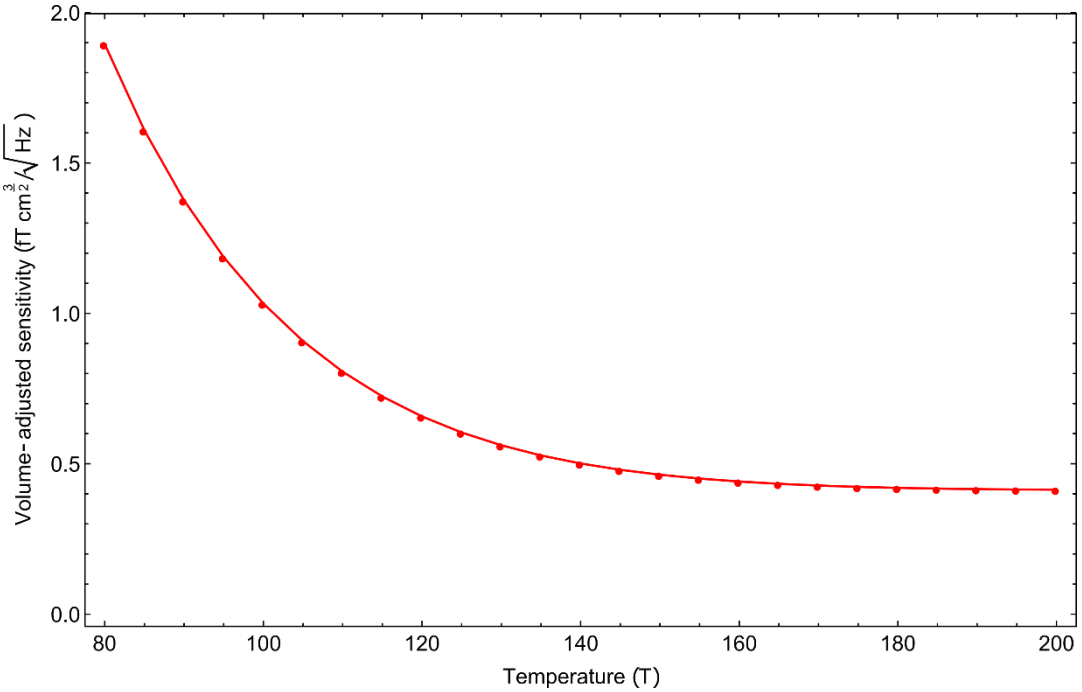

Figure 12: Optimal volume-adjusted projection-noise-limited sensitivity for a sub-mm active volume $V = \pi\ (200\ \mu m)^3$ *versus temperature.*

3.3 Pressure-induced glass bending

Since the buffer gas pressure that minimizes the full relaxation rate, as discussed in section 3.1, is about 10 bar or higher, it is important to estimate the magnitude of pressure induced glass bending due to the difference between external atmospheric pressure and the one inside the cavity microcells. In order to calculate this bending, we follow the classical theory of plates and shells [17]. Since we use Borofloat glass substrates with sub-mm thickness, we consider the approximation of a thin circular plate with supported edges, shown in Figure 13 (b). The bending depends on the distance *r* from the plate's centre, the thickness *t*, the total cross section *a* (radius for a circular plate) and the difference of pressure $\Delta\rho = \rho_{in} - \rho_{ex}$ between external and internal regions.

The total bending for a thin plate with supported edges is given by:

$$w(a,t,r) = \frac{\Delta\rho}{64D(t)}(a^2 - r^2)\left(\frac{(5+\nu_P)a^2}{1+\nu_P} - r^2\right) \qquad \text{Eq. 11}$$

where

$$D(t) = E_m t^3/12(1-{\nu_P}^2) \qquad \text{Eq. 12}$$

is the flexural rigidity, $\nu_P = 0.2$ and $E_m = 64 \times 10^9$ N/m^2 are the Borofloat Poisson ratio and Young's module, respectively. The maximum bending (r =0) obtained with Eq. 11 for supported edges is about 4 times bigger than the one for the condition with clamped edges.

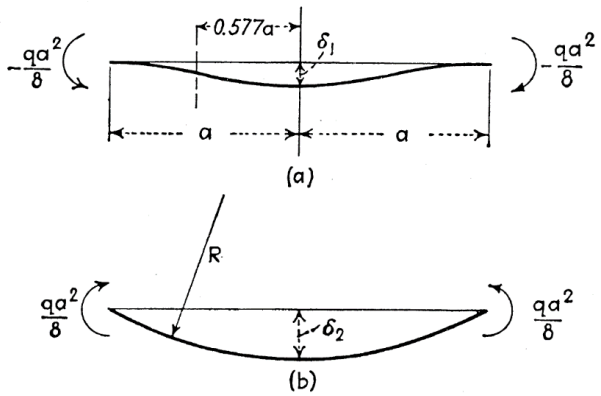

FIG. 30

Figure 13: Bending of thin circular plate with clamped (a) and supported (b) edges. (from [17]).

In Figure 14 we report the calculated glass bending with ρ_{in}=10 bar ($\Delta\rho = 10$ Pascal) for a thin plate of thickness 200 µm and *a*=200 µm (red), 500 µm (blue), 1 mm (green) and 1.75 mm (black), respectively. The maximum bending at the center of the glass plate ranges from 2 nm at *a*=200 µm up to 12 µm for *a*=1.75 mm. These values of *a* are the ones we choose as diameters of confining chambers in the cavity microcells. In order to avoid cylindrical lensing effects, we have designed round cavities to have a spherical symmetric bending. While the pressure induced bending corresponds to an effective change in cavity length and consequent resonant laser frequency, a change of about 0.5 GHz/nm, we expect this effect not to significantly change the pseudo collimated Gaussian mode of the planar cavity probe beam.

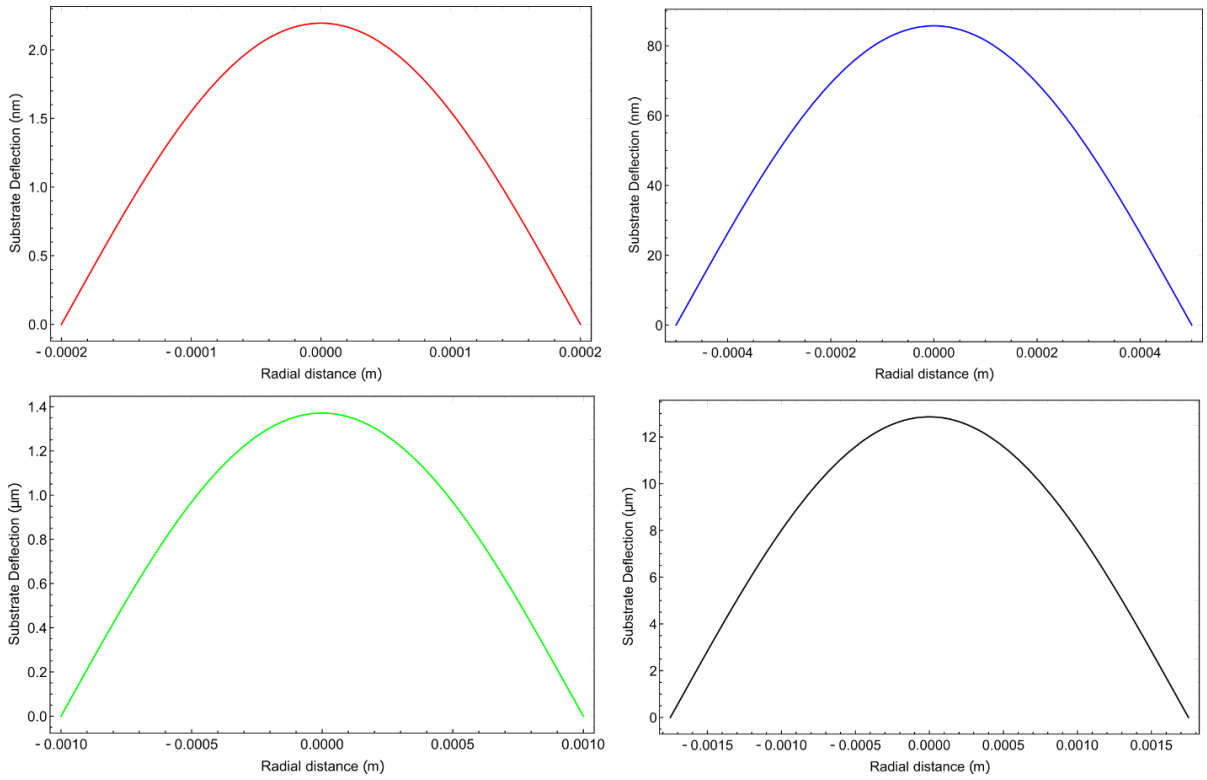

Figure 14: Glass substrate bending for 200 µm thickness and a=200 µm (red), 500 µm (blue), 1 mm (green) and 1.75 mm (black), respectively.

4 Design and fabrication of planar cavity microcells

Based on the parameter optimization described in Section 3, we have developed different designs of microcells, currently under fabrication by macQsimal leading partner CSEM.

4.1 Designs of planar cavity microcell

In Figure 15 we show the 4 designs of Silicon masks etched with 4, 9, 20 and 40 cavities, respectively. A large reservoir, with an area of 8mm x 8mm, is designed to enclose enough rubidium azide in liquid solution (up to 10 µl), which is then activated by UV illumination to get Rb vapour and N2 buffer gas with high pressure. The thickness of these Si masks, as well as the Borofloat substrates, is 200 µm. Multiple physics chambers, i.e., microcavities, are meant to perform a gradiometer measurement with sub-mm baseline. At the same time, due to total variation thickness of the wafers, some cavities may have a different length as well as better finesse. Having multiple cavities increases the chances to get high finesse and a cavity length close to the theoretical value of 600 µm.

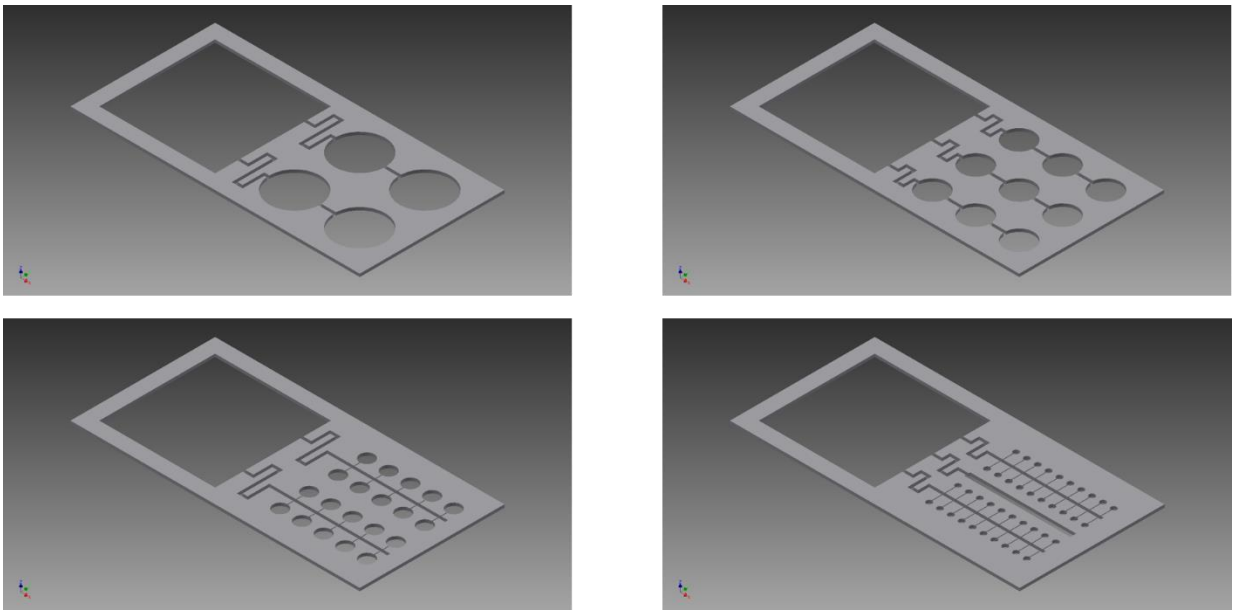

Figure 15: Designs of microcells with 4, 9, 20 and 40 cavities, respectively.

In Figure 16 we show the top view of the Si masks. The cavity diameter for the 4 designs is 3.5 mm, 2 mm, 1mm and 400 µm, for the 4 (a), 9 (b), 20 (c) and 40 (d) cavities designs, respectively. Three meanders with 200 µm width connect the large reservoir to the physics chambers, while secondary channels of 50 µm width connect the main channels to the physics chambers in the designs (c) and (d). Finally, design (d) also includes a physics rectangular channel, with 200 µm width, instead of round cavities as in all other designs.

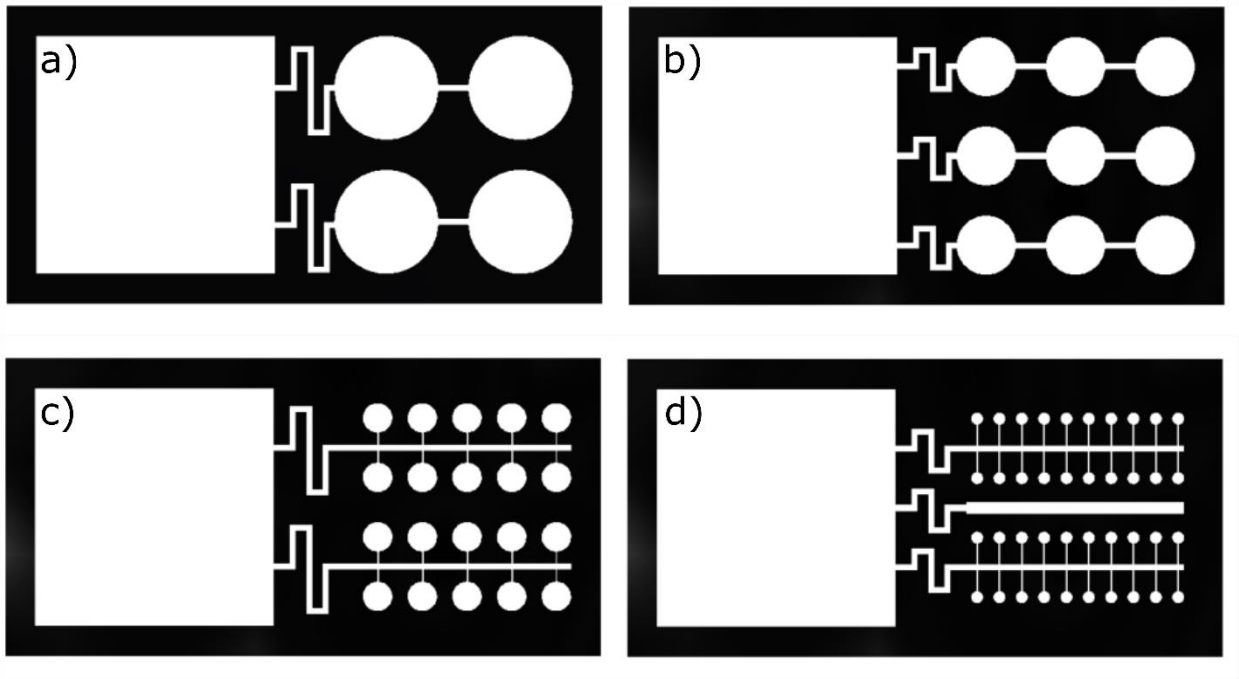

Figure 16: Top view. The reservoir is the squared area, while the round cavities are the physics chambers.

4.2 Fabrication steps

In Figure 17 we describe the fabrication steps of the cavity microcells, based on MEMS techniques, developed by macQsimal leading partner CSEM [18]. The fabrication process includes:

a) performing an anodic bonding between a first Borofloat® glass and a middle layer made of an etchable silicon material;

b) machining by wet etching the middle layer to define the different confining chambers, reservoir and connecting channels, wherein non-etched portions of the middle layer define the above-mentioned intermediate partition and contour walls laterally demarcating the confining chambers, and thus providing the illustrated pre-form;

c) filing the reservoir with a solution comprising an alkali metal compound, for example RbN_3, dissolved in at least one of its solvents, and evaporating said at least one solvent;

d) after water evaporation of those solvents, performing an anodic bonding between the filled preform, specifically between an upper face of the intermediate etched substrate, and a second Borofloat® glass substrate;

e) activation of the alkali compound, e.g., Rb and N_2, is performed. For example, Rb vapour and high pressure of buffer gas is released by UV illumination [18];

f) the outer surface of the top Borofloat® glass substrate is coated with the desired reflectance for probe and pump beam (high reflectance for probe and high transmittance for the pump);

g) the outer surface of the bottom Borofloat® glass substrate is coated with the desired reflectance for probe and pump beam (high reflectance for probe and high transmittance for the pump); The outer surfaces reflectance for the probe light can range between 90% and 99.99%, depending on the desired trade-off between finesse and residual absorption as well as on the measurement method, in transmission or reflection. The pump transmittance is 50% or higher, a partial reflection can be an advantage for full atomic polarization.

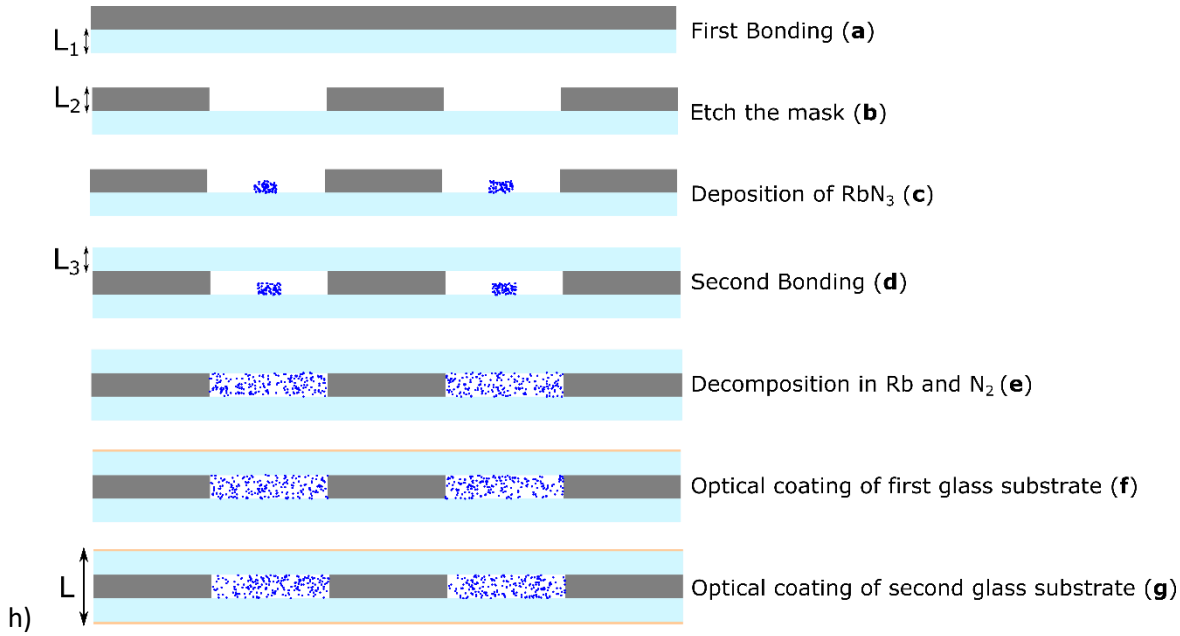

Figure 17: Fabrication steps of MEMS cavity microcells including final optical coating.

4.3 Coating of the microcells

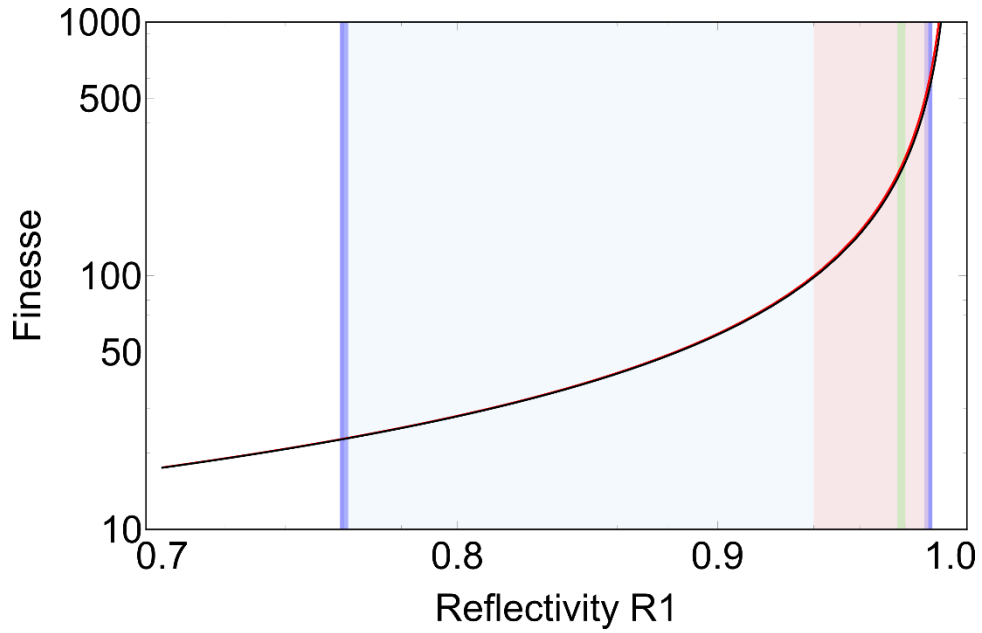

Figure 18: Cavity finesse versus laser-side reflectivity R1 at 780 nm, with the far side coating fixed at R2=99.9% (Red), or R2=99.8% (Black), to account for the 0.1% tolerance. By referring to Figure 3, the objective of the special coating on the outer surfaces of the microcells is to get high transmittivity at 795 nm, the pump beam wavelength, and high reflectivity at 780 nm, the probe beam wavelength, so that the microcell will also be an optical cavity for the probe beam, to enhance the light-matter interaction as well as the optical depth. While a coating with such step edge between two close wavelengths is not commercially available, we got a quote from the company Laseroptik to perform the experimental coating. The simulated performance of the coating is shown in Figure 19.

In Figure 18 we report the important figure of merit, the cavity finesse, versus the reflectivity R1 at 780 nm, when the backside coating is fixed to R2=99.9% (Red), or R2=99.8% (Black), given a 0.1% tolerance. These two curves mainly overlap while the change in R1 has a much bigger effect on Finesse.

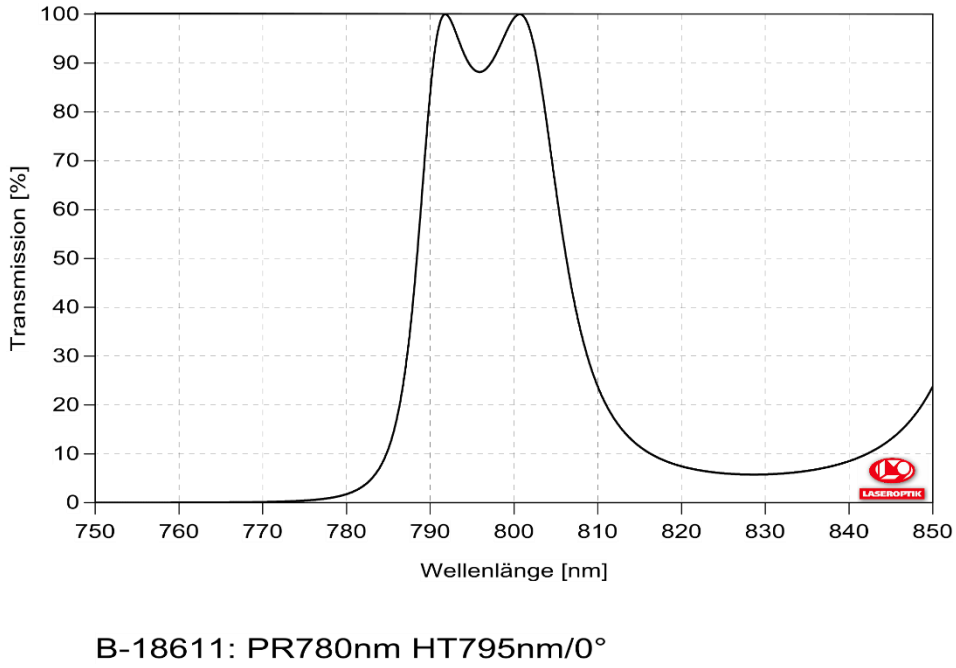

Figure 19: Best effort transmission for coating T1 vs wavelength. Parameters as in Figure 18, green line.

The green vertical line corresponds to the condition simulated by Laseroptik, close to the R1=97.8% at 780 nm (Finesse=270), while the blue vertical lines (enclosing the light-blue spread region) correspond to the worst-case scenario with either R1=76% or R1=99%. The latter deviation would give a finesse up to 500. The goal of the experimental coating is to have a cavity finesse between 100 and 500 at 780 nm probe light, while at the same time have a transmission close to 90% at 795 nm pump light.

5 Bibliography

[1] J. Kitching, "Chip-scale atomic devices," *Applied Physics Reviews,* vol. 5, p. 031302, 2018.

[2] D. Sheng et al., "Subfemtotesla scalar atomic magnetometry using multipass cells," *Physical Review Letters,* vol. 110, p. 160802, 2013.

[3] H. Crepaz et al., "Cavity enhanced atomic magnetometry," *Scientific Reports,* vol. 5, p. 15448, 2015.

[4] V. G. Lucivero, "A femtotesla quantum-noise-limited pulsed gradiometer at finite fields," in *OSA Quantum Information and Measurement*, Rome, 2019.

[5] M. Limes et al., "Portable magnetometry for detection of biomagnetism in ambient environments," *Physical Review Applied,* vol. 14, p. 011002, 2020.

[6] S. Li et al., "Optical rotation in excess of 100 rad generated by Rb vapor in a multipass cell," *Phys. Rev A,* vol. 84, p. 061403, 2011.

[7] V. Lucivero, “Femtotesla Direct Magnetic Gradiometer Using a Single Multipass Cell,” *Phys. Rev. Applied,* vol. 15, p. 014004, 2021.

[8] V. G. Lucivero et al., “Correlation function of spin noise due to atomic diffusion,” *Phys. Rev. A,* vol. 96, p. 062702, 2017.

[9] O. Hosten et al., “Measurement noise 100 times lower than the quantum-projection limit using entangled atoms,” *Nature,* vol. 529, pp. 505-508, 2016.

[10] C. Mazzinghi et al., “Cavity-enhanced atomic polarization rotation measurements,” *arXiv:2107.13302,* 2021.

[11] M. Zhu et al., “Fabry-Perot interferometer with picometer resolution referenced to an optical frequency comb,” *Optics and lasers in engineering,* vol. 67, pp. 128-134, 2015.

[12] J. Kitching et al., “NIST on a Chip: Realizing SI units with microfabricated alkali vapour cells,” *Journal of Physics: Conference Series,* vol. 723, p. 012056, 2016.

[13] M. T. Hummon et al., “Photonic chip for laser stabilization to an atomic vapor with 10^-11 instability,” *Optica,* vol. 5, pp. 443-449, 2018.

[14] S. J. Seltzer, Developments in alkali-metal atomic magnetometry, Princeton University, 2008.

[15] G. Colangelo et al., “Simultaneous tracking of spin angle and amplitude beyond classical limits,” *Nature,* vol. 543, pp. 525-528, 2017.

[16] C. Troullinou et al., “Squezed-light enhancement of sensitivity and signal bandwidth in an optically-pumped magnetometer,” *arXiv:2108.01519,* 2021.

[17] S. Timoshenko, Theory of plates and shells, McGraw-Hill Book Company, 1959.

[18] S. Karlen et al., “Lifetime assesment of RbN3-filled MEMS atomic vapor cells with Al2O3 coating,” *Optics Express,* vol. 3, p. 2187, 2017.